Observation of the Cosmic-ray Shadow of the Moon with IceCube

M. Santander – University of Alabama
et al.

Citation of published version:

Aartsen, M.G., et al. (2014): Observation of the Cosmic-ray Shadow of the Moon with IceCube. *Physical Review D,* 89(10).
DOI: http://dx.doi.org/10.1103/PhysRevD.89.102004

Observation of the cosmic-ray shadow of the Moon with IceCube

M. G. Aartsen,[2] R. Abbasi,[27] Y. Abdou,[22] M. Ackermann,[41] J. Adams,[15] J. A. Aguilar,[21] M. Ahlers,[27] D. Altmann,[9] J. Auffenberg,[27] X. Bai,[31,‡] M. Baker,[27] S. W. Barwick,[23] V. Baum,[28] R. Bay,[7] J. J. Beatty,[17,18] S. Bechet,[12] J. Becker Tjus,[10] K.-H. Becker,[40] M. Bell,[38] M. L. Benabderrahmane,[41] S. BenZvi,[27] J. Berdermann,[41] P. Berghaus,[41] D. Berley,[16] E. Bernardini,[41] A. Bernhard,[30] D. Bertrand,[12] D. Z. Besson,[25] G. Binder,[8,7] D. Bindig,[40] M. Bissok,[1] E. Blaufuss,[16] J. Blumenthal,[1] D. J. Boersma,[39,*] S. Bohaichuk,[20] C. Bohm,[34] D. Bose,[13] S. Böser,[11] O. Botner,[39] L. Brayeur,[13] H.-P. Bretz,[41] A. M. Brown,[15] R. Bruijn,[24] J. Brunner,[41] M. Carson,[22] J. Casey,[5] M. Casier,[13] D. Chirkin,[27] A. Christov,[21] B. Christy,[16] K. Clark,[38] F. Clevermann,[19] S. Coenders,[1] S. Cohen,[24] D. F. Cowen,[38,37] A. H. Cruz Silva,[41] M. Danninger,[34] J. Daughhetee,[5] J. C. Davis,[17] C. De Clercq,[13] S. De Ridder,[22] P. Desiati,[27] M. de With,[9] T. DeYoung,[38] J. C. Díaz-Vélez,[27] M. Dunkman,[38] R. Eagan,[38] B. Eberhardt,[28] J. Eisch,[27] R. W. Ellsworth,[16] S. Euler,[1] P. A. Evenson,[31] O. Fadiran,[27] A. R. Fazely,[6] A. Fedynitch,[10] J. Feintzeig,[27] T. Feusels,[22] K. Filimonov,[7] C. Finley,[34] T. Fischer-Wasels,[40] S. Flis,[34] A. Franckowiak,[11] R. Franke,[41] K. Frantzen,[19] T. Fuchs,[19] T. K. Gaisser,[31] J. Gallagher,[26] L. Gerhardt,[8,7] L. Gladstone,[27] T. Glüsenkamp,[41] A. Goldschmidt,[8] G. Golup,[13] J. G. Gonzalez,[31] J. A. Goodman,[16] D. Góra,[41] D. T. Grandmont,[20] D. Grant,[20] A. Groß,[30] C. Ha,[8,7] A. Haj Ismail,[22] P. Hallen,[1] A. Hallgren,[39] F. Halzen,[27] K. Hanson,[12] D. Heereman,[12] D. Heinen,[1] K. Helbing,[40] R. Hellauer,[16] S. Hickford,[15] G. C. Hill,[2] K. D. Hoffman,[16] R. Hoffmann,[40] A. Homeier,[11] K. Hoshina,[27] W. Huelsnitz,[16,§] P. O. Hulth,[34] K. Hultqvist,[34] S. Hussain,[31] A. Ishihara,[14] E. Jacobi,[41] J. Jacobsen,[27] K. Jagielski,[1] G. S. Japaridze,[4] K. Jero,[27] O. Jlelati,[22] B. Kaminsky,[41] A. Kappes,[9] T. Karg,[41] A. Karle,[27] J. L. Kelley,[27] J. Kiryluk,[35] F. Kislat,[41] J. Kläs,[40] S. R. Klein,[8,7] J.-H. Köhne,[19] G. Kohnen,[29] H. Kolanoski,[9] L. Köpke,[28] C. Kopper,[27] S. Kopper,[40] D. J. Koskinen,[38] M. Kowalski,[11] M. Krasberg,[27] K. Krings,[1] G. Kroll,[28] J. Kunnen,[13] N. Kurahashi,[27] T. Kuwabara,[31] M. Labare,[13] H. Landsman,[27] M. J. Larson,[36] M. Lesiak-Bzdak,[35] M. Leuermann,[1] J. Leute,[30] J. Lünemann,[28] J. Madsen,[33] R. Maruyama,[27] K. Mase,[14] H. S. Matis,[8] F. McNally,[27] K. Meagher,[16] M. Merck,[27] P. Mészáros,[37,38] T. Meures,[12] S. Miarecki,[8,7] E. Middell,[41] N. Milke,[19] J. Miller,[13] L. Mohrmann,[41] T. Montaruli,[21,‖] R. Morse,[27] R. Nahnhauer,[41] U. Naumann,[40] H. Niederhausen,[35] S. C. Nowicki,[20] D. R. Nygren,[8] A. Obertacke,[40] S. Odrowski,[30] A. Olivas,[16] M. Olivo,[10] A. O'Murchadha,[12] L. Paul,[1] J. A. Pepper,[36] C. Pérez de los Heros,[39] C. Pfendner,[17] D. Pieloth,[19] E. Pinat,[12] N. Pirk,[41] J. Posselt,[40] P. B. Price,[7] G. T. Przybylski,[8] L. Rädel,[1] M. Rameez,[21] K. Rawlins,[3] P. Redl,[16] R. Reimann,[1] E. Resconi,[30] W. Rhode,[19] M. Ribordy,[24] M. Richman,[16] B. Riedel,[27] J. P. Rodrigues,[27] C. Rott,[17,¶] T. Ruhe,[19] B. Ruzybayev,[31] D. Ryckbosch,[22] S. M. Saba,[10] T. Salameh,[38] H.-G. Sander,[28] M. Santander,[27,†] S. Sarkar,[32] K. Schatto,[28] M. Scheel,[1] F. Scheriau,[19] T. Schmidt,[16] M. Schmitz,[19] S. Schoenen,[1] S. Schöneberg,[10] A. Schönwald,[41] A. Schukraft,[1] L. Schulte,[11] O. Schulz,[30] D. Seckel,[31] Y. Sestayo,[30] S. Seunarine,[33] C. Sheremata,[20] M. W. E. Smith,[38] D. Soldin,[40] G. M. Spiczak,[33] C. Spiering,[41] M. Stamatikos,[17,**] T. Stanev,[31] A. Stasik,[11] T. Stezelberger,[8] R. G. Stokstad,[8] A. Stößl,[41] E. A. Strahler,[13] R. Ström,[39] G. W. Sullivan,[16] H. Taavola,[39] I. Taboada,[5] A. Tamburro,[31] A. Tepe,[40] S. Ter-Antonyan,[6] G. Tešić,[38] S. Tilav,[31] P. A. Toale,[36] S. Toscano,[27] M. Usner,[11] D. van der Drift,[8,7] N. van Eijndhoven,[13] A. Van Overloop,[22] J. van Santen,[27] M. Vehring,[1] M. Voge,[11] M. Vraeghe,[22] C. Walck,[34] T. Waldenmaier,[9] M. Wallraff,[1] R. Wasserman,[38] Ch. Weaver,[27] M. Wellons,[27] C. Wendt,[27] S. Westerhoff,[27] N. Whitehorn,[27] K. Wiebe,[28] C. H. Wiebusch,[1] D. R. Williams,[36] H. Wissing,[16] M. Wolf,[34] T. R. Wood,[20] K. Woschnagg,[7] C. Xu,[31] D. L. Xu,[36] X. W. Xu,[6] J. P. Yanez,[41] G. Yodh,[23] S. Yoshida,[14] P. Zarzhitsky,[36] J. Ziemann,[19] S. Zierke,[1] and M. Zoll[34]

(IceCube Collaboration)

[1]*III. Physikalisches Institut, RWTH Aachen University, D-52056 Aachen, Germany*
[2]*School of Chemistry and Physics, University of Adelaide, Adelaide, South Australia 5005, Australia*
[3]*Department of Physics and Astronomy, University of Alaska Anchorage, 3211 Providence Drive, Anchorage, Alaska 99508, USA*
[4]*CTSPS, Clark-Atlanta University, Atlanta, Georgia 30314, USA*
[5]*School of Physics and Center for Relativistic Astrophysics, Georgia Institute of Technology, Atlanta, Georgia 30332, USA*
[6]*Department of Physics, Southern University, Baton Rouge, Louisiana 70813, USA*
[7]*Department of Physics, University of California, Berkeley, California 94720, USA*
[8]*Lawrence Berkeley National Laboratory, Berkeley, California 94720, USA*
[9]*Institut für Physik, Humboldt-Universität zu Berlin, D-12489 Berlin, Germany*
[10]*Fakultät für Physik & Astronomie, Ruhr-Universität Bochum, D-44780 Bochum, Germany*
[11]*Physikalisches Institut, Universität Bonn, Nussallee 12, D-53115 Bonn, Germany*
[12]*Science Faculty CP230, Université Libre de Bruxelles, B-1050 Brussels, Belgium*
[13]*Vrije Universiteit Brussel, Dienst ELEM, B-1050 Brussels, Belgium*
[14]*Department of Physics, Chiba University, Chiba 263-8522, Japan*

[15]*Department of Physics and Astronomy, University of Canterbury, Private Bag 4800, Christchurch 8140, New Zealand*
[16]*Department of Physics, University of Maryland, College Park, Maryland 20742, USA*
[17]*Department of Physics and Center for Cosmology and Astroparticle Physics, Ohio State University, Columbus, Ohio 43210, USA*
[18]*Department of Astronomy, Ohio State University, Columbus, Ohio 43210, USA*
[19]*Department of Physics, TU Dortmund University, D-44221 Dortmund, Germany*
[20]*Department of Physics, University of Alberta, Edmonton, Alberta T6G 2E1, Canada*
[21]*Département de physique nucléaire et corpusculaire, Université de Genève, CH-1211 Genève, Switzerland*
[22]*Department of Physics and Astronomy, University of Gent, B-9000 Gent, Belgium*
[23]*Department of Physics and Astronomy, University of California, Irvine, California 92697, USA*
[24]*Laboratory for High Energy Physics, École Polytechnique Fédérale, CH-1015 Lausanne, Switzerland*
[25]*Department of Physics and Astronomy, University of Kansas, Lawrence, Kansas 66045, USA*
[26]*Department of Astronomy, University of Wisconsin, Madison, Wisconsin 53706, USA*
[27]*Department of Physics and Wisconsin IceCube Particle Astrophysics Center, University of Wisconsin, Madison, Wisconsin 53706, USA*
[28]*Institute of Physics, University of Mainz, Staudinger Weg 7, D-55099 Mainz, Germany*
[29]*Université de Mons, 7000 Mons, Belgium*
[30]*T.U. Munich, D-85748 Garching, Germany*
[31]*Bartol Research Institute and Department of Physics and Astronomy, University of Delaware, Newark, Delaware 19716, USA*
[32]*Department of Physics, University of Oxford, 1 Keble Road, Oxford OX1 3NP, United Kingdom*
[33]*Department of Physics, University of Wisconsin, River Falls, Wisconsin 54022, USA*
[34]*Oskar Klein Centre and Department of Physics, Stockholm University, SE-10691 Stockholm, Sweden*
[35]*Department of Physics and Astronomy, Stony Brook University, Stony Brook, New York 11794-3800, USA*
[36]*Department of Physics and Astronomy, University of Alabama, Tuscaloosa, Alabama 35487, USA*
[37]*Department of Astronomy and Astrophysics, Pennsylvania State University, University Park, Pennsylvania 16802, USA*
[38]*Department of Physics, Pennsylvania State University, University Park, Pennsylvania 16802, USA*
[39]*Department of Physics and Astronomy, Uppsala University, P.O. Box 516, S-75120 Uppsala, Sweden*
[40]*Department of Physics, University of Wuppertal, D-42119 Wuppertal, Germany*
[41]*DESY, D-15735 Zeuthen, Germany*

(Received 29 May 2013; published 28 May 2014)

We report on the observation of a significant deficit of cosmic rays from the direction of the Moon with the IceCube detector. The study of this "Moon shadow" is used to characterize the angular resolution and absolute pointing capabilities of the detector. The detection is based on data taken in two periods before the completion of the detector: between April 2008 and May 2009, when IceCube operated in a partial configuration with 40 detector strings deployed in the South Pole ice, and between May 2009 and May 2010 when the detector operated with 59 strings. Using two independent analysis methods, the Moon shadow has been observed to high significance ($> 6\sigma$) in both detector configurations. The observed location of the shadow center is within 0.2° of its expected position when geomagnetic deflection effects are taken into account. This measurement validates the directional reconstruction capabilities of IceCube.

DOI: 10.1103/PhysRevD.89.102004 PACS numbers: 96.50.S-, 95.85.Ry, 96.20.-n, 29.40.Ka

[*]Corresponding author.
boersma@icecube.wisc.edu
[†]Corresponding author.
santander@icecube.wisc.edu
[‡]Present address: Physics Department, South Dakota School of Mines and Technology, Rapid City, South Dakota 57701, USA.
[§]Present address: Los Alamos National Laboratory, Los Alamos, New Mexico 87545, USA.
[‖]Also at Sezione INFN, Dipartimento di Fisica, I-70126 Bari, Italy.
[¶]Present address: Department of Physics, Sungkyunkwan University, Suwon 440-746, Korea.
[**]Present address: NASA Goddard Space Flight Center, Greenbelt, Maryland 20771, USA.

I. INTRODUCTION

IceCube is a km^3-scale Cherenkov detector deployed in the glacial ice at the geographic South Pole. Its primary goal is to search for astrophysical sources of high-energy neutrinos. A major background for this search is the high rate of atmospheric muons produced when cosmic rays with energies above a few TeV interact with the Earth's atmosphere. The rate of muon events in IceCube above several hundred GeV dominates the total trigger rate of the detector, and is approximately six orders of magnitude higher than the rate of neutrino-induced events.

The incoming direction of multi-TeV cosmic muons is on average within 0.1° of the arrival direction of the primary cosmic-ray particle [1]. This implies that the distribution of incoming muons should mimic the almost isotropic distribution of TeV cosmic rays in the sky [2,3]. An important feature of the angular distribution of cosmic rays is the presence of a relative deficit in the flux of cosmic rays coming from the direction of the Moon. This effect, due to the absorption of cosmic rays by the Moon, was first predicted by Clark in 1957 [4], and its observation has been used by several experiments as a way of calibrating the angular resolution and the pointing accuracy of their particle detectors (see [5–8], or [9] for recent results.)

For IceCube, the Moon shadow analysis is a vital and unique verification tool for the track reconstruction algorithms that are used in the search for point-like sources of astrophysical neutrinos [10], among other analyses. In this paper we will report on the observation of the Moon shadow using data taken between April 2008 and May 2010, before the completion of the IceCube Neutrino Observatory in December 2010.

Two independent analysis methods were used in the search for the Moon shadow. The first analysis performs a binned, one-dimensional search for the Moon shadow that compares the number of events detected from the direction of the Moon to the number of background events recorded at the same declination as the Moon but at a different right ascension. The second method uses an unbinned, two-dimensional maximum-likelihood algorithm that retrieves the best fit value for the total number of events shadowed by the Moon.

Both methods show consistent results, and constitute the first statistically significant detection of the shadow of the Moon using a high-energy neutrino telescope.

II. DETECTOR CONFIGURATION AND DATA SAMPLE

A. The IceCube detector

The IceCube neutrino telescope uses the deep Antarctic ice as a detection medium. High-energy neutrinos that interact with nucleons in the ice produce relativistic leptons that emit Cherenkov radiation as they propagate through the detector volume. This Cherenkov light is detected by a volumetric array of 5160 digital optical modules (DOMs) deployed at depths between 1450 and 2450 m below the ice surface. Each DOM consists of a 25 cm diameter photomultiplier tube (PMT) [11] and the electronics for signal digitization [12] housed inside a pressure-resistant glass sphere.

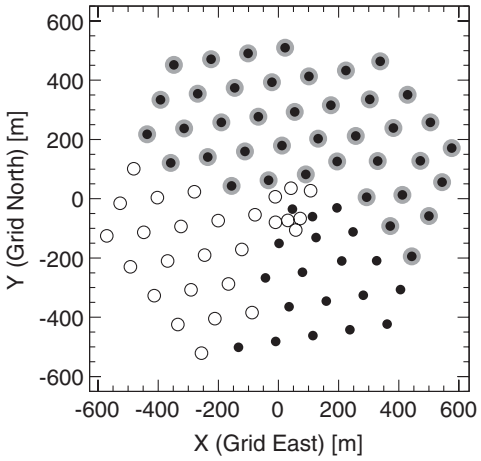

FIG. 1. Layout of the two detector configurations considered in this analysis. IC40 (gray) operated between 2008 and 2009. The deployment of more strings initiated the IC59 configuration (black) operated between 2009 and 2010. The remaining strings that form the final 86-string configuration, the last of them installed in December 2010, are shown as open circles. The *y* axis (Grid North) is aligned with the Greenwich Prime Meridian.

The DOMs are attached to 86 strings that provide mechanical support, electrical power, and a data connection to the surface. Consecutive DOMs in each string are vertically separated by a distance of about 17 m, while the horizontal spacing between strings is about 125 m. A compact group of eight strings with a smaller spacing between DOMs is located at the bottom of the detector and forms DeepCore [13], which is designed to extend the energy reach of IceCube to lower neutrino energies. The IceTop surface array, devoted to the detection of extensive air showers from cosmic rays with energies between 300 TeV and 1 EeV, completes the instrumentation of the observatory.

The construction of IceCube began in 2005 and was completed in December 2010. During construction, the detector operated in several partial configurations. Data from two different configurations were used in this paper: between 2008 and 2009 the detector operated with 40 strings deployed in the ice (IC40), and between 2009 and 2010 the detector operated in its 59-string configuration (IC59). The layout of the two detector configurations used in this work can be seen in Fig. 1.

B. Data sample

In order to reduce the rate of noise-induced events, IceCube DOMs are operated in a coincidence mode called hard local coincidence (HLC). During the operation of

IC40 and IC59 the HLC requirement was met if photon hits were detected within a ± 1 μs window in the two nearest neighbor or next-to-nearest neighbor DOMs. The detection of HLC hits leads to a full readout and transmission to the surface of the digitized PMT signals. A trigger condition is then used to combine these photon hits into a candidate event. The main trigger in IceCube is a simple multiplicity trigger called SMT8 that requires HLC hits in eight DOMs within 5 μs. For each trigger, all HLC hits within a ± 10 μs window are recorded and merged into a single event.

The majority of events detected by IceCube are due to down-going muons produced in the interaction of high-energy cosmic rays with the Earth's atmosphere. During the operation of IC40, the cosmic muon-induced trigger rate was about 1.1 kHz, which increased to about 1.7 kHz during the IC59 data-taking period. This high rate of cosmic-ray muon events provides a high-statistics data set that can be used to search for the Moon shadow.

Since the rate of data transfer from the South Pole via the South Pole archival and data exchange satellite communication system is limited to about 100 Gb per day, only a limited number of muon events can be transmitted north over the satellite. For this reason, the data used in this analysis were taken using a dedicated online filter that selects only events passing minimum quality cuts and reconstructed within a predefined angular acceptance window around the Moon.

A fast likelihood-based muon track reconstruction [14] is performed at the South Pole to obtain the arrival direction of each event. The reconstructed direction of the muon track is then compared to the position of the Moon in the sky, which is calculated using the publicly available `SLALIB` library of astronomical routines [15].

An event satisfies the Moon filter selection criterium if at least 12 DOMs in 3 different strings record photon hits, and if the reconstructed direction is within 10° of the Moon position in declination and $40°/\cos(\delta_\mu)$ in right ascension (where δ_μ is the declination of the event and the cosine factor accounts for projection effects).

The filter is enabled when the Moon is at least 15° above the horizon. Due to the particular geographic location of IceCube at the South Pole, the Moon rises above this threshold only once per month, as its elevation above the horizon changes slowly over the course of days. Since the number of muon events recorded by IceCube is a strong function of the elevation angle, the rate of events that pass the acceptance window condition changes during this period as this window follows the apparent motion of the Moon at the South Pole. The strong correlation between the Moon elevation and rate of events passing the Moon filter is shown in Fig. 2. The maximum event rate is also modulated over a longer time scale of 18.6 years (known as the lunar draconic period [16]) in which the maximum elevation of the Moon above the horizon at the South Pole oscillates between the extreme values of 18.4 and 28.4°. The maximum Moon

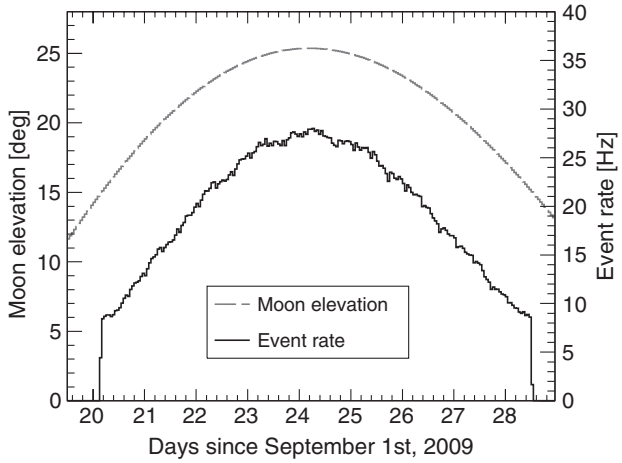

FIG. 2. Rate of muon events passing the Moon filter during the month of September 2009, when IceCube was operating in its IC59 configuration. The correlation between the Moon elevation (dashed line) and event rate (solid line) is clearly visible.

elevation during the IC40 data-taking period was 26.9°, while for IC59 it was 25.6°. Approximately 1.29×10^8 muon events passing the Moon filter condition were recorded during the IC40 data-taking period, and about 1.77×10^8 events were recorded during the operation of the IC59 configuration.

Once these events have been transferred from the South Pole, an iterative maximum-likelihood reconstruction algorithm is applied to the data set to obtain a more precise track direction [14]. The algorithm also determines the angular uncertainty in the reconstructed track direction by mapping the likelihood space around the best track solution and fitting it with a paraboloid function [17]. A narrow paraboloid indicates a precise reconstruction, while a wide paraboloid indicates a larger uncertainty in the reconstructed direction of the muon track. The 1σ contour line of the paraboloid function defines an error ellipse for the reconstructed direction of the track. In this analysis, a single, one-dimensional estimator of the uncertainty is obtained by calculating the root-mean-square (rms) value of the semimajor axes of that error ellipse.

The likelihood-based track reconstruction algorithm used in this work is based on the leading-edge times of the first light pulses recorded by each DOM. For the fast track reconstruction at the South Pole the single-photoelectron (SPE) fit is used. In this fit, the likelihood that the first photon arrived at the pulse leading-edge times is maximized. The photons arriving at later times are ignored.

Neutrino point source searches rely on the multiphotoelectron (MPE) fit. In the MPE fit, the total number of photoelectrons N_d in each DOM, d, is taken into account by multiplying the likelihood that a photon was detected at the first leading-edge time with the probability that the remaining $N_d - 1$ photons arrived later [14]. For bright, i.e. high-energy, events in simulated data the MPE fit results in a

slightly better angular resolution than the SPE fit. Also, the number of direct (unscattered) photons associated with the reconstructed track tends to be larger with the MPE fit than with the SPE fit. This makes this quantity as well as related quantities more effective for selecting well-reconstructed events. The MPE fit is discussed further in Sec. V B 2.

The track reconstruction algorithms use the local detector coordinate system and the direction of a reconstructed track is given as a zenith and azimuth angle. Using the event times as recorded by the data acquisition system, these are transformed into a right ascension, α_μ, and declination, δ_μ, which are the more natural variables for searches of neutrino point-like sources.

III. SIMULATION

A. Cosmic-ray energy and composition

The muons produced in the interaction between the cosmic rays and the atmosphere must traverse several kilometers of ice before reaching the IceCube detector, losing energy in the process. This sets a lower limit of several hundred GeV on the energy of the muons at the ground level that would trigger the detector. By extension, the primary cosmic-ray particle needed to produce this kind of muon should have an energy of at least several TeV. In the following, we will refer to the energy of the primary cosmic ray, not the muons, unless specified otherwise.

Given that this analysis deals with cosmic-ray showers near the energy threshold of the detector, the number of muons produced in each shower that reaches the detector is small. Most events in the Moon data sample are composed of one or two energetic muons, and only 2% of the events have muon multiplicities higher than ten.

The detailed energy scale for the IC40 and IC59 data sets was determined using simulated cosmic-ray air showers created with the CORSIKA Monte Carlo code [18] using the SIBYLL model of high-energy hadronic interactions [19]. The chemical composition and spectral shape of the cosmic rays generated in this simulation follow the polygonato model [20].

From these simulations, we estimate that the median energy of the primary cosmic rays that trigger the IceCube detector is 20 TeV, while the median energy of events that satisfy the Moon filter condition is about 40 TeV for both IC40 and IC59, with 68% of the events between 10 and 200 TeV. The increased median energy of the filtered sample is due to the greater average zenith angles of the cosmic rays that pass the filter, which requires primary particles with enough energy to produce muons able to traverse more ice and trigger IceCube. The muons produced by cosmic rays passing the Moon filter have a mean energy of about 2 TeV at the ground level and reach the detector with a mean energy of 200 GeV. The mean muon energy also depends on the zenith angle, and increases from 2.5 TeV for a zenith angle of 65° (the maximum elevation of the Moon) to 5.6 TeV for a zenith angle of 75° (the minimum elevation of the Moon for which data is recorded.) This dependence is shown in Fig 3.

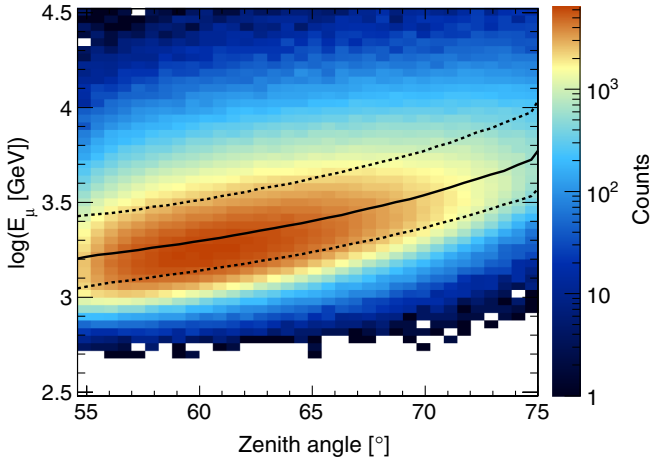

FIG. 3 (color online). Muon energy at the ground level as a function of the zenith angle for events passing the Moon filter condition. The solid line indicates the median muon energy in each zenith bin, while the 68% containing interval is defined between the two dashed lines. The monotonic increase in muon energy with the zenith angle is a consequence of the larger ice overburden for very inclined events, which raises the initial muon energy necessary to reach the detector.

The energy spectrum of all primary cosmic rays triggering the IceCube detector is shown in Fig. 4 and compared to the spectrum of those that pass the Moon filter. Also shown in the figure are the five main chemical elements (protons, He, C, O, and Fe) that make more than 95% of the Moon filter data sample assuming the polygonato composition model. The two main components of the sample are proton (68% of the events) and helium (23%).

As will be described in the following subsection, an important quantity for calculating the deflection of cosmic rays in the magnetic field of the Earth is the particle rigidity $R \sim E/Z$, for a particle with the energy E and electric charge Z. The distribution of magnetic rigidities for the sample is given in Fig. 4 for reference.

B. Geomagnetic field effects

Cosmic rays with TeV energies should experience a small deflection in their trajectories due to the influence of the magnetic field of the Earth as they propagate towards the detector. This deflection would appear in the Moon shadow analysis as a shift in the position of the shadow with respect to the true Moon position, which could be wrongly interpreted as a systematic offset produced by the event reconstruction.

In order to quantify this offset and compare it with any possible shift observed in the data, we have developed a particle propagation code that can be used to trace cosmic rays in the geomagnetic field. Using this code, particles are

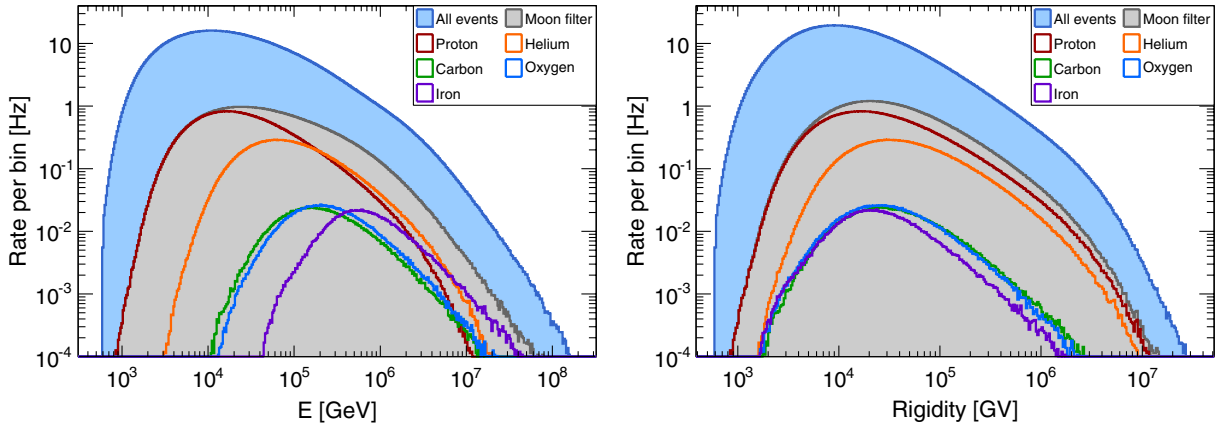

FIG. 4 (color online). Differential event rate as a function of cosmic-ray primary energy (left) and rigidity (right) for all events in IC59 (light blue) and for only those passing the Moon filter (gray) as determined from simulation studies. The main chemical elements that make up the events passing the Moon filter are shown with lines of different color. The width of the histogram bins is 0.014 in $\log_{10}(\text{energy, rigidity})$. The IC40 configuration shows a similar energy response.

propagated radially outwards from the South Pole up to a a distance of 30 Earth radii from the center of the Earth at which point the opening angle between the initial and final velocity vectors is computed. This angle gives the magnitude of the deflection in the geomagnetic field.

We use the international geomagnetic reference field (IGRF) model [21] to calculate deflections. In this model, the field is calculated using a truncated multipole series expansion. The current revision of the model, IGRF-11, can be used to calculate B-field values through 2015, providing a good coverage of the time range over which the data were taken. The model is accessible through a library of `FORTRAN` routines called `GEOPACK` developed by N. Tsyganenko.[1]

The IGRF-11 model describes what is known as the *internal* magnetic field of the Earth, which is presumably produced by electric currents in the outer core of the planet and accounts for most of the total magnetic field. A weaker component, known as the *external* field, is produced by electrical currents in the ionosphere. The external component is not included in our calculation since it only modifies the total angular deflection by a few percent while significantly increasing the computation time needed to perform the simulation.

In our simulation, primary cosmic rays are propagated in the direction of the Moon as seen from the South Pole for different times during the data-taking period. The cosmic-ray energy and chemical composition is sampled from the event distributions that pass the Moon filter, shown in Fig. 4. The resulting total deflection $\Delta\lambda$ is shown in Fig. 5 as a function of energy for 10^5 simulated cosmic-ray particles for the five main chemical elements that contribute to the Moon data set. The energy and charge dependence of the deflection angle is evident in the plot. Different bands in the plot correspond to different chemical elements. The width of each band is due to particles that were propagated in different directions in the sky (i.e. through different regions of the Earth's magnetic field) experiencing different deflections. A power-law fit to the simulation results has been performed to estimate the deflection angle as a function of energy and charge. The fit gives a good agreement for the following expression:

$$\Delta\lambda[^\circ] = 1.9^\circ \frac{Z}{E[\text{TeV}]} \sim \frac{1.9^\circ}{R[\text{TV}]}, \tag{1}$$

where Z is the charge of the cosmic ray (CR) in units of the elementary charge e, E is its energy in TeV, and $\Delta\lambda$ is given in degrees. This expression has the same functional form as the one found in [22] with a higher normalization in our simulation, which could be due to the difference in geographic location and other simulation details. The

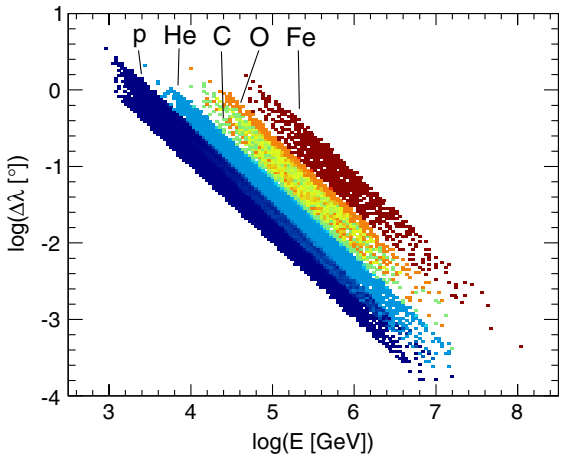

FIG. 5 (color online). Angular deflection as a function of energy for the different chemical elements simulated using the particle propagation code described in Sec. III B.

[1] http://geo.phys.spbu.ru/~tsyganenko/modeling.html.

deflection angle is also given as a function of the rigidity R of the cosmic ray in teravolts (TV).

The deflection of each cosmic ray with the arrival direction (α_μ, δ_μ) in sidereal coordinates is calculated with respect to the position of the Moon at the time of the event $(\alpha_{\rm Moon}, \alpha_{\rm Moon})$. The two coordinates that characterize the position of an event in this system are a right ascension difference, $\Delta\alpha = (\alpha_\mu - \alpha_{\rm Moon})\cos\delta_\mu$, and a declination difference, $\Delta\delta = \delta_\mu - \delta_{\rm Moon}$, with respect to the nominal Moon position. The median shift in the right ascension $\Delta\alpha$ for all CR particles in our simulation is 0.08°, with 68% of the particles having deflection angles in the interval $0.02° < \Delta\alpha < 0.24°$. The median shift in the declination $\Delta\delta$ is consistent with 0°, with 68% of the events contained in the interval $|\Delta\delta| < 0.04°$. Propagation tests performed using only the dipole term of the geomagnetic field instead of the full IGRF model produce similar results.

The cosmic-ray muons that ultimately trigger IceCube are also deflected by the geomagnetic field. However, given the typical energies of the muons (about 2 TeV), their total track length (in the 50–100 km range), and their charge distribution, their contribution to the total deflection angle is typically below ∼0.01°. For this reason, the muon contribution has been ignored in calculating the expected total deflection angle.

The direction of muons propagating through the ice is smeared due to multiple Coulomb scattering (MCS). Given the typical muon energies and the thickness of the ice overburden, we estimate that the average rms opening angle for deflections due to MCS is about 0.05°. This smearing is much smaller than the angular resolution of IceCube for muons in this energy range (typically between 0.5 and 0.9°) and is already included in the estimate of the angular resolution from simulation studies given in Secs. IV and V.

IV. BINNED ANALYSIS

A. Description of the method

The main goal of the binned analysis is to obtain a profile view of the Moon shadow and measure its width, which can be used as a direct estimator of the angular resolution of the event reconstruction. This is accomplished by comparing the observed number of events as a function of angular distance from the Moon to an estimate of how many events would have been observed if there was no shadow.

For this comparison, the angular distance between the reconstructed muon tracks and the expected position of the Moon is binned in constant increments of 0.2° up to a maximum angular distance of 5°. This defines the so-called *on-source* distribution of events. The same binning procedure is applied to eight *off-source* regions centered around points located at the same declination as the Moon, but offset from it in the right ascension by ±5°, ±10°, ±15°, and ±20°, where it is assumed that the shadowing effect is negligible. The average number of counts as a function of radius for these eight off-source regions represents the expectation in the case of no Moon shadow.

The relative difference between the number of events in the ith bin in the on-source region $N_i^{\rm on}$, and the average number of events in the same bin in the off-source regions $\langle N_i^{\rm off}\rangle$ is calculated using the following expression:

$$\frac{\Delta N_i}{\langle N\rangle_i} = \frac{N_i^{\rm on} - \langle N_i^{\rm off}\rangle}{\langle N_i^{\rm off}\rangle}. \tag{2}$$

The uncertainty in the relative difference is given by

$$\sigma_{\Delta N/\langle N\rangle} = \frac{N_i^{\rm on}}{\langle N_i^{\rm off}\rangle}\sqrt{\frac{1}{N_i^{\rm on}} + \frac{1}{s\langle N_i^{\rm off}\rangle}}, \tag{3}$$

where $s = 8$ is the number of off-source regions. The distribution of relative differences as a function of angular radius from the Moon constitutes a profile view of the shadow.

Simulation studies indicate that the point spread function (PSF) of the detector can be approximated with a two-dimensional Gaussian function. We use this approximation to obtain an estimate of the angular resolution of the track reconstruction by fitting the distribution of $\Delta N_i/\langle N\rangle_i$ for the events in the Moon data set.

Following [23], we treat the Moon as a point-like cosmic-ray sink that removes $\Phi\pi R_M^2$ events from the muon sample, where R_M is the angular radius of the Moon ($R_M \sim 0.26°$) and Φ is the cosmic-ray flux at the location of the Moon in units of events per square degree. This deficit is smeared by the PSF of our detector, resulting in a radially symmetric two-dimensional Gaussian distribution of shadowed events. The differential density of shadowed events per solid angle, Ω,can be expressed as

$$\frac{dN}{d\Omega} = -\frac{\Phi R_M^2}{2\sigma^2}\, e^{-\psi^2/2\sigma^2}, \tag{4}$$

where ψ is the radial distance from the center of the Moon. The number of shadowed events in the ith bin of the width $\Delta\psi$ can be calculated by integrating the differential event density over the bin annulus in polar coordinates (ψ, ϕ):

$$N_s(\psi_i) = \int_0^{2\pi}\int_{\psi_i-\Delta\psi/2}^{\psi_i+\Delta\psi/2} \psi\frac{dN}{d\Omega}\, d\psi\, d\phi \tag{5}$$

$$\approx -\frac{\Phi\pi R_M^2\Delta\psi}{\sigma^2}\psi_i e^{-\psi_i^2/2\sigma^2}. \tag{6}$$

The number of events, N_e, that would have been observed in the same bin with no shadowing is $2\pi\Phi\psi_i\Delta\psi$. The ratio of Eqs. (6) and N_e gives us the expected distribution of relative differences $\Delta N_i/\langle N\rangle_i$ for a detector with a Gaussian PSF of the angular resolution σ:

TABLE I. Optimal bin radius (ψ_b), the number of observed events in the on-source ($N^b_{\rm on}$) and off-source ($N^b_{\rm off}$) bins, the event deficit in the on-source bin (ΔN), and the statistical significance of the deficit for the binned analysis of IC40 and IC59 data sets.

	IC40	**IC59**
ψ_b	0.75°	0.79°
$N^b_{\rm on}$	52967	96412
$N^b_{\rm off}$	54672	100442
ΔN	−1705	−4030
Significance	6.9σ	12.1σ

$$\frac{N_s}{N_e}(\psi_i) = -\frac{R_M^2}{2\sigma^2} e^{-\psi_i^2/2\sigma^2}. \quad (7)$$

This expression is used to fit the experimental data. The only free parameter in the fit is σ, which is used as the estimator for the angular resolution of the experimental data set. The value obtained from the fit can be compared to the expected angular resolution obtained from simulation studies. Following previous Moon shadow studies [8,23], we use the Gaussian σ parameter as the estimator instead of a 68% containing radius used elsewhere in the literature.

Our treatment ignores the finite angular size of the lunar disc, which may affect the result of the fit. However, since the expected angular resolution (of the order 1°) is several times larger than the angular radius of the Moon, we expect that the effect should influence the fit value of σ only at the few-percent level.

A set of cuts was developed to optimize for the statistical significance of the detection of the Moon shadow. Under the assumption of Poisson statistics, the relation between the significance S, the fraction η of events passing the cuts, and the resulting median angular resolution $\Psi_{\rm med}$ after cuts is

$$S \propto \frac{\sqrt{\eta}}{\Psi_{\rm med}}. \quad (8)$$

The optimization of the cuts was performed on the CORSIKA-simulated air showers described in Sec. III. Two cut variables were used in this analysis: the angular uncertainty σ_i in the reconstruction of the muon track direction estimated individually for each event, and the reduced log likelihood *rlogl*, which is the log likelihood for the best track solution divided by the number of degrees of freedom in the fit. The number of degrees of freedom in the track fit is equal to the number of DOMs triggered by the event minus the number of free parameters in the fit (five for this fit). Both *rlogl* and σ are standard cut variables used in the search for point-like sources of astrophysical neutrinos [10], the search for a diffuse flux of high-energy neutrinos [24], and several other analyses of IceCube data.

Once the cuts have been determined, the number of events falling inside a circular search bin around the Moon is compared to the number of events contained in a bin of the same angular radius for the average off-source region. The statistical significance of an observed deficit in the number of events in the search bin is calculated using the method given by [25].

The optimal radius of the search bin ψ_b can be found by maximizing the S' parameter in the following expression:

$$S'(\psi_s) \propto \frac{\int_0^{\psi_s} \psi' {\rm PSF}(\psi') d\psi'}{\psi_s}, \quad (9)$$

where ψ_s is the radius of the bin and ${\rm PSF}(\psi')$ is the point spread function of the detector after cuts obtained from simulations. Due to its symmetry, the PSF has already been integrated over the azimuthal coordinate and only the radial dependence remains. The optimization of the search bin radius is also performed using simulated CORSIKA showers generated for each detector configuration.

B. Results

A set of cuts was determined independently for both the IC40 and IC59 detector configurations using the optimization procedure described above on simulated data. For IC40, only events with $rlog < 9$ and $\sigma_i < 1.01°$ were used in the analysis, with 26% of the events surviving the cuts.

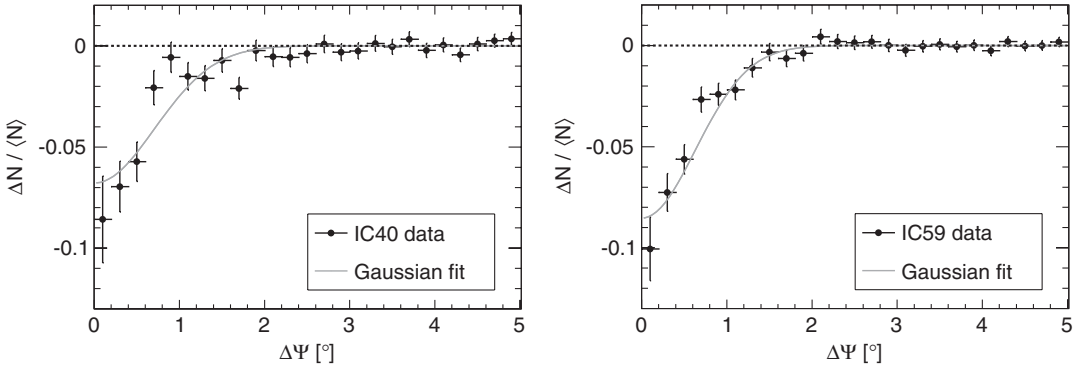

FIG. 6. Relative difference between the number of events in the *on-source* and the average *off-source* region as a function of the angular distance from the nominal position of the Moon for the IC40 *(left)* and IC59 *(right)* data sets. A Gaussian fit to the deficits is shown in gray.

TABLE II. Gaussian angular resolution σ obtained from the fit to the Moon shadow profile shown in Fig. 6. The χ^2/dof of the fit is also given for the two results.

	IC40	IC59
σ	$0.71° \pm 0.07°$	$0.63° \pm 0.04°$
χ^2/dof	31.4/24	13.0/24

After cuts, the median angular resolution of the reconstruction was estimated from simulation to be 0.93°, with 68% of the events having angular uncertainties, σ_i, between 0.38 and 2.18°. A two-dimensional fit to the simulated data shows that for the Gaussian approximation the corresponding resolution σ is about 0.74°.

In the case of IC59, the events selected for the analysis were those with $rlog < 8.8$ and $\sigma_i < 1.04°$, which resulted in a passing rate of 34%. The median resolution after cuts was 0.78°, with the 68% containing interval located between 0.33° and 1.78°, with a Gaussian width, σ, of about 0.71°.

After the cuts were applied to both data sets, the radius of the optimal search bin (ψ_b) and the number of events contained in that bin for both the on-source (N^b_{on}) and off-source (N^b_{off}) windows was calculated. In both detector configurations, a deficit in the number of events in the on-source bin when compared to the off-source bin was observed at high statistical significance ($> 6\sigma$), as expected due to the shadowing effect of the Moon. A complete list of the number of events observed on each bin, the observed deficit in the on-source bin, as well as the statistical significance associated with such a deficit, is given in Table I.

The Moon shadow profile shown in Fig. 6 was fit using the expression given in Eq. (7), where σ is the only free parameter. A list of fit results is given in Table II. In both cases, the observed angular resolution shows good agreement with the one obtained from the above-mentioned simulation studies.

V. UNBINNED ANALYSIS

A. Description of the method

The second algorithm used to search for the Moon shadow is based on an unbinned maximum-likelihood method analogous to that used in the search for point-like sources of high-energy neutrinos [26]. This kind of likelihood analysis was first proposed in [27], and was applied for the first time to a Moon shadow search in [28].

The goal of the unbinned analysis is to determine the most likely location of the Moon shadow to compare it with the expected location after accounting for magnetic deflection effects. An agreement between the observed and expected positions of the shadow center will serve as an important confirmation of the absolute pointing accuracy of the detector.

The analysis is also used to obtain the most likely number of events shadowed by the Moon, which can be compared to the expectation. An essential ingredient in the unbinned analysis is an event-wise estimation of the angular error. Both systematic underestimation and overestimation of this error would lead to a shallower apparent shadow than expected. The number of shadowed events is a free parameter in this analysis and the comparison with the expected number of shadowed events is effectively a test of the angular uncertainty estimate.

In this analysis [29,30], the position of each muon event is defined with respect to the Moon position in the coordinate system $(\Delta\alpha, \Delta\delta)$ that was defined in Sec. III B. Only events with $|\Delta\delta| \leq 8°$ and $|\Delta\alpha + \alpha_{\text{off}}| \leq 8°$ were considered in the analysis, where $\alpha_{\text{off}} = 0°$ defines the on-source region, and $\alpha_{\text{off}} = \pm 18°$ defines two off-source regions.

A set of quality cuts was determined for this analysis using the same simulation data set as in the one-dimensional binned case. The same variables were used in the optimization of the cuts: the angular reconstruction uncertainty σ_i, and the reduced log likelihood of each event $rlogl$.

The analysis method assumes that the data can be described as a linear combination of signal and background components, where the relative contribution from each component is established by a maximum-likelihood fit to the data. For a data set containing N events, the log-likelihood function is defined as

$$\log \mathcal{L}(n_s, \vec{x}_s) = \sum_{i=1}^{N} \log\left[\frac{n_s}{N}\mathcal{S}(\vec{x}_i, \sigma_i; \vec{x}_s) + \left(1 - \frac{n_s}{N}\right)\mathcal{B}(\vec{x}_i)\right], \tag{10}$$

where $\mathcal{S}$ and $\mathcal{B}$ are the signal and background probability density functions (PDFs), n_s is the unknown number of signal events, or in this case the total number of shadowed events, and $\vec{x}_s$ is the unknown central position of the

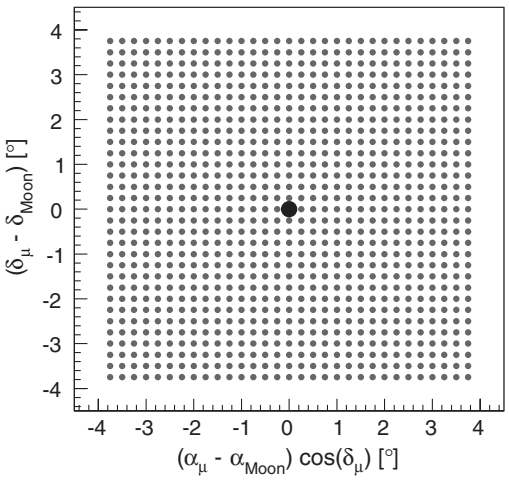

FIG. 7. Search grid in $(\Delta\alpha, \Delta\delta)$ as used in the unbinned likelihood analysis. A value of n_s is determined for each one of the points in the grid. The nominal location of the Moon is shown as a black square at $\vec{x}_s = (0, 0)$.

TABLE III. Description of the cuts used in the unbinned analysis. Percentages indicate the relative fraction of events that survive the cut with respect to the previous selection criterium.

	IC40	IC59
Events before cuts	18.8×10^6	22.2×10^6
Cut 1: $0.075° < \sigma_i < 1.5°$	50%	58%
Cut 2: $6.5 <$ rlogl < 8	89%	91%
Events after cuts	8.4×10^6	11.7×10^6

shadow of the Moon, relative to the nominal position of the Moon. Note that since the expected signal in the case of the Moon is a deficit in the muon flux rather than an excess, n_s should be negative. In the absence of a geomagnetic field, the shadow should occur exactly on the nominal position of the Moon, i.e. $\vec{x}_s = (0, 0)$, but according to the estimates described in Sec. III B we expect the shadow to be shifted by about 0.1°.

The signal PDF for each event is modeled using a two-dimensional Gaussian distribution around the reconstructed direction $\vec{x}_i$ of the muon track:

$$\mathcal{S}(\vec{x}_i, \sigma_i; \vec{x}_s) = \frac{1}{2\pi\sigma_i^2} e^{\frac{-|\vec{x}_i - \vec{x}_s|^2}{2\sigma_i^2}}, \tag{11}$$

where the width of the Gaussian distribution σ_i is the angular reconstruction uncertainty obtained on an event-by-event basis by the paraboloid algorithm described in Sec. II B.

The background PDF is assumed to depend only on $\Delta\delta$, and is derived from the distribution of reconstructed declination angles for the muon tracks contained in the two off-source regions.

The best fit values for the number of signal events in the data n_s and the shift of the shadow center $\vec{x}_s$ are determined by maximizing the log-likelihood function (10). Besides $\vec{x}_s$ and n_s, the width and overall shape of the shadow are also of interest. In searches for point sources of high-energy neutrinos [26], for all points $\vec{x}_s$ on a fine grid covering the sky, the value of n_s is determined which maximizes the likelihood function. Similarly, in the Moon shadow analysis we determine the value of n_s that maximizes the likelihood function (10) on a rectangular grid of 961 values for $\vec{x}_s = (\Delta\alpha_s, \Delta\delta_s)$. This 31×31 grid is defined inside a window with a size of $|\Delta\delta| \leq 4°$ and $|\Delta\alpha| \leq 4°$ shown in Fig. 7.

In order to avoid edge effects, all events in the $8° \times 8°$ on-source region are taken into account in the maximum-likelihood calculation.

The statistical significance associated with each value of n_s can then be calculated by applying the same likelihood analysis to the two off-source regions. The rms spread of the resulting distribution of n_s values for those regions gives an estimate of the 1σ spread expected in the case of a null detection. Using this estimate, each point in the on-source region can be given a statistical significance by taking the ratio between the value of n_s at that point and the 1σ estimate from the off-source regions.

The observed value of n_s is compared to an estimate of the true number of CRs shadowed by the Moon. This estimate is obtained by counting the number of events that fall within a circular window with the same radius as the Moon but located in the off-source region.

B. Results

1. SPE analysis

The cuts used in the unbinned analysis are listed in Table III. The resulting median angular resolution of the IC40 and IC59 data sets was estimated by applying those same cuts to simulated cosmic-ray events. In the case of IC40, the median angular resolution is 1.13°, with 68% of the events having angular uncertainties, σ_i, between 0.48° and 2.63°. For IC59, the median resolution is 0.98°, with a 68% containing interval defined between 0.38 and 2.23°.

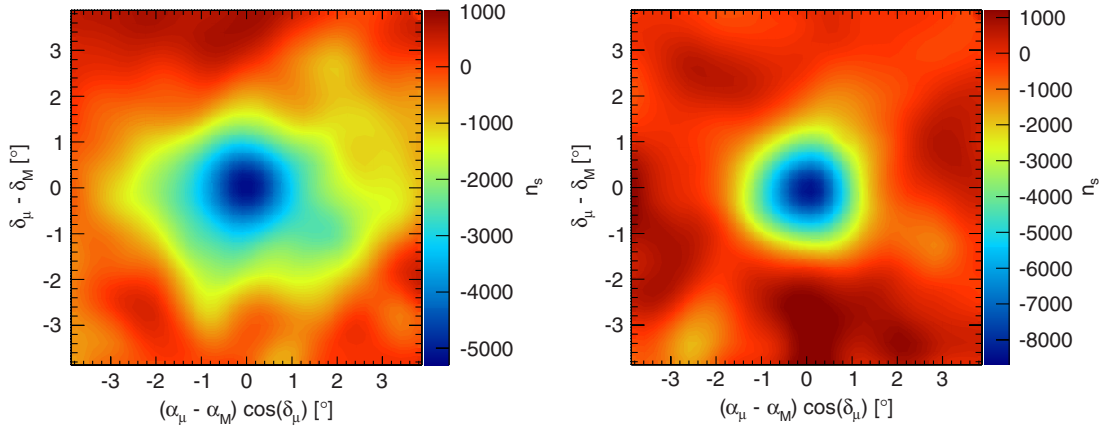

FIG. 8 (color online). Contour plot of the value of n_s in the $(\Delta\alpha, \Delta\delta)$ coordinate system for on-source regions of the IC40 (left) and IC59 data sets (right).

TABLE IV. Unbinned analysis results detailing the observed and expected deficit counts from the Moon for IC40 and IC59. The observed deficits and the $(\Delta\alpha, \Delta\delta)$ offsets are given for the most likely position of the Moon shadow as determined by the maximum-likelihood fit.

	IC40	IC59
Observed deficit	5320 ± 501	8700 ± 550
Expected deficit	5734 ± 76	8192 ± 91
Off-source rms	521	627
Significance	10.2σ	13.9σ
$\Delta\alpha$	$-0.02°$	$0.06°$
$\Delta\delta$	$0.08°$	$0.00°$

As described in the previous section, the maximum-likelihood values of n_s were calculated on a grid around the position of the Moon for both sets. The contour maps of the n_s values obtained for IC40 and IC59 are shown in Fig. 8, where the shadowing effect of the Moon is visible as a strong deficit in the central regions of the maps. The deepest deficit observed with both detector configurations is in good agreement with the expected number of shadowed events, listed in Table IV. Using the rms spread of the off-source regions as a 1σ estimator in the case of a null detection, we calculated the statistical significance of the observation by taking the ratio of the largest deficit observed to the rms spread, which is also shown in Table IV. The shadow of the Moon is observed in both the IC40 and IC59 data sets to a high statistical significance ($> 10\sigma$).

In order to obtain a better estimate of the position of the minimum of the shadow, a finer grid with a spacing of about 0.016° was used in the central $\pm 0.4° \times \pm 0.4°$ region around the Moon. Using this grid, we obtain the positions indicated in Table IV as offsets in right ascension ($\Delta\alpha$) and declination ($\Delta\delta$) with respect to the nominal position of the Moon in the sky. The shadow positions for both detector configurations are shown in Fig. 9 together with 1σ, 2σ, and 3σ contours. The expected location of the minimum after accounting for geomagnetic deflection effects is also given for comparison. In both detector configurations, the observed position of the minimum is consistent with its expected location to within statistical fluctuations. These measurements imply that, on average, the absolute pointing accuracy of the detector during the IC40 and IC59 data-taking periods was better than about 0.2°.

2. MPE analysis

The unbinned analysis was also applied to IC59 events reconstructed using the MPE algorithm and its corresponding angular error estimate described in Sec. II B. In simulations, the MPE fit performs better than the SPE reconstruction thanks to its more realistic description of the arrival times of multiple photons at each DOM. However, at high energies the algorithm can be confused by stochastic energy losses that occur along the muon track and are not described in the likelihood function implemented in the MPE algorithm. This usually results in an underestimation of the angular uncertainty on the reconstructed direction of the track. In practice, this problem can be solved by rescaling the average pull (the ratio between the real and estimated angular errors as obtained from simulation studies) to unity. The MPE version of the unbinned analysis was used as a verification of this correction technique.

Simulation studies indicate an average pull of 1.55 for the MPE reconstruction, versus 1.0 for SPE. Without correcting for this underestimation of the angular error in the MPE fit, the Moon shadow analysis resulted in a minimum value for n_s of 3574 ± 434 shadowed events, differing by more than 5 standard deviations from the expectation of 6373 ± 80. Redoing this analysis with the

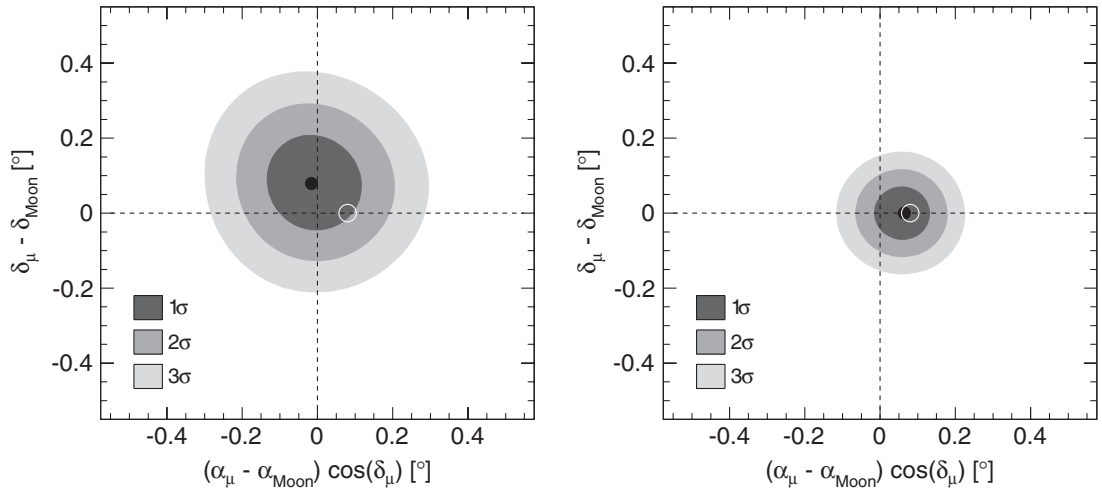

FIG. 9. Contour plot for the position of the minimum of the Moon shadow in the IC40 (left) and IC59 data (right) in the $(\Delta\alpha, \Delta\delta)$ coordinate system. The reconstructed position for the Moon shadow from the maximum-likelihood analysis is shown as a black point, while the expected position of the Moon shadow after accounting for magnetic deflection is shown as a white circle.

angular error estimates rescaled by a factor of 1.55 resulted in a fitted n_s value compatible with expectation, validating the pull correction method.

In neutrino analyses, where the range of muon energies is much larger than in the Moon analysis sample, the applied MPE pull correction is energy dependent, instead of using only the average value of the pull for the entire data set.

VI. CONCLUSIONS

The shadow of the Moon in TeV cosmic rays has been detected to a high significance ($> 6\sigma$) using data taken with the IC40 and IC59 configurations of the IceCube neutrino observatory. For both detector configurations, the observed positions of the shadow minimum show good agreement with expectations given the statistical uncertainties. An important implication of this observation is that any systematic effects introduced by the detector geometry and the event reconstruction on the absolute pointing capabilities of IceCube are smaller than about 0.2°.

The average angular resolution of both data samples was estimated by fitting a Gaussian function to the shadow profile. In both cases, the 1σ width of the Moon shadow was found to be about 0.7°, which is in good agreement with the expected angular resolution based on simulation studies of down-going muons.

The total number of shadowed events estimated using the unbinned analysis is also consistent with expectations for IC40 and IC59. This provides an indirect validation of the angular uncertainty estimator obtained from the reconstruction algorithm. This is especially relevant for the MPE analysis, where simulation studies indicate that the uncertainty estimator has to be rescaled in order to avoid underestimating the true angular error. Applying this correction factor to the data results in a number of shadowed events compatible with expectation.

Note that the value of the average angular resolution determined in this analysis is *not* a direct measurement of the point spread function to be used in searches for point sources of high-energy neutrinos. Rather, the agreement of this value with the value estimated from our simulations should be seen as an experimental verification of our simulation and the methods used to estimate the angular uncertainty of individual track reconstructions. This angular uncertainty depends on several factors, in particular on the energy with which the muon traverses the detector. As the energy distribution for neutrino analyses differs from that of the Moon shadow analysis, the average angular resolution may be better or worse, but can reliably be estimated from our simulation.

ACKNOWLEDGMENTS

We acknowledge the support from the following agencies: the U.S. National Science Foundation, Office of Polar Programs, the U.S. National Science Foundation, Physics Division, the University of Wisconsin Alumni Research Foundation, the Grid Laboratory of Wisconsin (GLOW) grid infrastructure at the University of Wisconsin, Madison, the Open Science Grid (OSG) grid infrastructure; the U.S. Department of Energy, the National Energy Research Scientific Computing Center, the Louisiana Optical Network Initiative (LONI) grid computing resources; the Natural Sciences and Engineering Research Council of Canada, WestGrid and Compute/Calcul Canada; the Swedish Research Council, the Swedish Polar Research Secretariat, the Swedish National Infrastructure for Computing (SNIC), and the Knut and Alice Wallenberg Foundation, Sweden; the German Ministry for Education and Research (BMBF), Deutsche Forschungsgemeinschaft (DFG), the Helmholtz Alliance for Astroparticle Physics (HAP), the Research Department of Plasmas with Complex Interactions (Bochum), Germany; the Fund for Scientific Research (FNRS-FWO), FWO Odysseus programme, the Flanders Institute to encourage scientific and technological research in industry (IWT), the Belgian Federal Science Policy Office (Belspo); the University of Oxford, United Kingdom; the Marsden Fund, New Zealand; the Australian Research Council; the Japan Society for Promotion of Science (JSPS); and the Swiss National Science Foundation (SNSF), Switzerland.

[1] R. Abbasi *et al.* (IceCube Collaboration), Phys. Rev. D **87**, 012005 (2013).
[2] R. Abbasi *et al.* (IceCube Collaboration), Astrophys. J. Lett. **718**, L194 (2010).
[3] R. Abbasi *et al.* (IceCube Collaboration), Astrophys. J. Lett. **740**, 16 (2011).
[4] G. W. Clark, Phys. Rev. **108**, 450 (1957).
[5] M. Ambrosio *et al.* (MACRO Collaboration), Astropart. Phys. **20**, 145 (2003).
[6] P. Achard, O. Adriani, M. Aguilar-Benitez, M. van den Akker, J. Alcaraz, G. Alemanni, J. Allaby, A. Aloisio, M. G. Alviggi, and H. Anderhub (L3 Collaboration), Astropart. Phys. **23**, 411 (2005).
[7] A. Oshima, S. R. Dugad, U. D. Goswami, S. K. Gupta, Y. Hayashi, N. Ito, A. Iyer, P. Jagadeesan, A. Jain, and S. Kawakami (GRAPES-3 Collaboration), Astropart. Phys. **33**, 97 (2010).
[8] P. Adamson *et al.* (MINOS Collaboration), Astropart. Phys. **34**, 457 (2011).

[9] B. Bartoli *et al.* (ARGO-YBJ Collaboration), Phys. Rev. D **84**, 022003 (2011).
[10] R. Abbasi *et al.* (IceCube Collaboration), Astrophys. J. **732**, 18 (2011).
[11] R. Abbasi *et al.* (IceCube Collaboration), Nucl. Instrum. Methods Phys. Res., Sect. A **618**, 139 (2010).
[12] R. Abbasi *et al.* (IceCube Collaboration), Nucl. Instrum. Methods Phys. Res., Sect. A **601**, 294 (2009).
[13] R. Abbasi *et al.* (IceCube Collaboration), Astropart. Phys. **35**, 615 (2012).
[14] J. Ahrens *et al.* (AMANDA Collaboration), Nucl. Instrum. Methods Phys. Res., Sect. A **524**, 169 (2004).
[15] P. Wallace, ASP Conf. Ser. **61**, 481 (1994).
[16] *Encyclopedia of Astronomy and Astrophysics*, edited by R. A. Meyers and S. N. Shore (Academic Press, New York, 1989).
[17] T. Neunhöffer, Astropart. Phys. **25**, 220 (2006).
[18] D. Heck *et al.*, *CORSIKA: A Monte Carlo Code to Simulate Extensive Air Showers*, Technical Report No. FZKA 6019 (Forschungszentrum Karlsruhe, 1998).
[19] E.-J. Ahn, R. Engel, T. Gaisser, P. Lipari, and T. Stanev, Phys. Rev. D **80**, 094003 (2009).
[20] J. R. Hörandel, Astropart. Phys. **19**, 193 (2003).
[21] C. C. Finlay *et al.*, Geophys. J. Int. **183**, 1216 (2010).
[22] G. D. Sciascio and R. Iuppa, *Proceedings of the 2nd Roma International Conference on Astroparticle Physics (RICAP), Rome, Italy, 2009* [Nucl. Instrum. Methods Phys. Res., Sect. A **630**, 63 (2011)].
[23] J. H. Cobb *et al.* (Soudan 2 Collaboration), Phys. Rev. D **61**, 092002 (2000).
[24] R. Abbasi *et al.* (IceCube Collaboration), Phys. Rev. D **84**, 082001 (2011).
[25] T.-P. Li and Y.-Q. Ma, Astrophys. J. **272**, 317 (1983).
[26] J. Braun, J. Dumm, F. D. Palma, C. Finley, A. Karle, and T. Montaruli, Astropart. Phys. **29**, 299 (2008).
[27] W. W. Kinnison *et al.*, Phys. Rev. D **25**, 2846 (1982).
[28] M. Wascko, Ph. D. thesis, University of California, Riverside, 2001.
[29] J. Blumenthal, Diploma thesis, Rheinisch-Westfälische Technische Hochschule (RWTH) Aachen, 2011.
[30] R. Reimann, Diploma thesis, Rheinisch-Westfälische Technische Hochschule (RWTH) Aachen, 2011.